



**HAL**  
open science

## Where does subduction initiate and cease? A global scale perspective

Martina M Ulvrova, Nicolas Coltice, Simon Williams, Paul J Tackley

► **To cite this version:**

Martina M Ulvrova, Nicolas Coltice, Simon Williams, Paul J Tackley. Where does subduction initiate and cease? A global scale perspective. *Earth and Planetary Science Letters*, 2019, 528, pp.115836. 10.1016/j.epsl.2019.115836 . hal-03228622

**HAL Id: hal-03228622**

**<https://hal.science/hal-03228622>**

Submitted on 18 May 2021

**HAL** is a multi-disciplinary open access archive for the deposit and dissemination of scientific research documents, whether they are published or not. The documents may come from teaching and research institutions in France or abroad, or from public or private research centers.

L'archive ouverte pluridisciplinaire **HAL**, est destinée au dépôt et à la diffusion de documents scientifiques de niveau recherche, publiés ou non, émanant des établissements d'enseignement et de recherche français ou étrangers, des laboratoires publics ou privés.

**1 Where does subduction initiate and cease? A global  
2 scale perspective.**

Martina M. Ulvrova<sup>1</sup>, Nicolas Coltice<sup>2</sup>, Simon Williams<sup>3</sup>, and Paul J.

Tackley<sup>1</sup>

---

Corresponding author: M. Ulvrova, Department of Earth Sciences, Institute of Geophysics,  
ETH Zürich, Sonneggstrasse 5, Zürich, 8092, Switzerland. (martina.ulvrova@erdw.ethz.ch)

<sup>1</sup>Institute of Geophysics, Department of  
Earth Sciences, ETH Zürich, Zürich,  
Switzerland.

<sup>2</sup>Laboratoire de Géologie, École Normale  
Supérieure, CNRS-UMR 8538, PSL  
Research University, Paris, France

<sup>3</sup>EarthByte Group, School of Geosciences,  
University of Sydney, Sydney, New South  
Wales, Australia

3 **Abstract.** The thermo-mechanical evolution of the Earth's mantle is largely  
4 controlled by the dynamics of subduction zones, which connect the surface  
5 tectonic plates with the interior. However, little is known about the system-  
6 atics of where subduction starts and stops within the framework of global  
7 plate motions and evolving continental configurations. Here, we investigate  
8 where new subduction zones preferentially form, and where they endure and  
9 cease using statistical analysis of large-scale simulations of mantle convec-  
10 tion that feature self-consistent plate-like lithospheric behaviour and con-  
11 tinental drift in the spherical annulus geometry. We juxtapose the results of  
12 numerical modelling with subduction histories retrieved from plate tectonic  
13 reconstruction models and from seismic tomography. Numerical models show  
14 that subduction initiation is largely controlled by the strength of the litho-  
15 sphere and by the length of continental margins (for 2D models, the num-  
16 ber of continental margins). Strong lithosphere favors subduction inception  
17 in the vicinity of the continents while for weak lithosphere the distribution  
18 of subduction initiation follows a random process distribution. Reconstruc-  
19 tions suggest that subduction initiation and cessation on Earth is also not  
20 randomly distributed within the oceans, and more subduction zones cease  
21 in the vicinity of continental margins compared to subduction initiation. Our  
22 model results also suggest that intra-oceanic subduction initiation is more  
23 prevalent during times of supercontinent assembly (e.g. Pangea) compared  
24 to more recent continental dispersal, consistent with recent interpretations  
25 of relict slabs in seismic tomography.

## 1. Introduction

26 Subduction of the rigid plates is a fundamental process in Earth evolution, allowing  
27 chemical cycling between the surface and the deep mantle [Kerrick, 2001]. Indeed, the  
28 surface and interior of the planet are interconnected within a self-organized system in  
29 which subduction arises from an instability of the top boundary layer, while it also induces  
30 convective currents and pulls tectonic plates [Lowman, 2011; Coltice et al., 2017]. The  
31 evolution of the lithospheric plates including continents is then characterized by repeating  
32 Wilson cycles during which ocean basins periodically close and open while supercontinents  
33 assemble and disperse. However, little is known about subduction inception in the set-  
34 ting of global tectonics with floating continental rafts. How far from the continents do  
35 new subduction zones preferentially form? How do plate motions influence subduction  
36 inception? At which locations with respect to the position of the continental margins do  
37 subduction zones cease?

38 Few examples of active subduction inception or cessation are available to study. Young  
39 subduction systems can be found at the Mussau Trench [Hegarty et al., 1982] and Yap  
40 Trench [Lee, 2004] in the western Pacific, but it is not clear if these will develop into self-  
41 sustained subduction. Much of our knowledge on how subduction starts and stops is based  
42 on the geological record, including marine studies of forearcs [Reagan et al., 2010] and  
43 on-land studies of ophiolites [Dilek and Furnes, 2009], and on numerical modelling [e.g.  
44 Nikolaeva et al., 2010]. These studies indicate that subduction may initiate in a diverse  
45 range of tectonic settings; at passive margins [Nikolaeva et al., 2010], fracture zones such as  
46 for example Aleutian subduction zone [Maffione et al., 2017], at extinct spreading centres

47 such as for example Puysegur [Lebrun et al., 2003], adjacent to fossil island arcs [Leng  
48 and Gurnis, 2015], triggered by plumes [Gerya et al., 2015], or where mantle suction flow  
49 occurs [Baes et al., 2018]. Stern [2004] proposes two distinct mechanisms for subduction  
50 initiation: spontaneous nucleation by e.g. foundering at passive margins, or induced  
51 initiation involving forced convergence of existing plates.

52 In common with subduction initiation, cessation of subduction has been attributed to a  
53 variety of mechanisms, including collision with continents or oceanic plateaus, interaction  
54 between the subduction zone and spreading ridges and transforms, or within the context  
55 of a broader-scale reorganisation of plate motions [e.g. Michaud et al., 2006]. Some ac-  
56 tive subduction systems undergo a so-called polarity reversal, when the overriding plate  
57 becomes the subducting plate and vice versa. In such a case, subduction initiation and  
58 termination are directly related. An example of reversal of an active convergent boundary  
59 is the New Hebrides with the reversal of subduction of the Pacific beneath the Australian  
60 plate at the Vitiaz trench [Auzende et al., 1988].

61 A limiting factor in our current knowledge on subduction is the reliance on geological  
62 evidence collected on land, for example where former intra-oceanic subduction products  
63 have been accreted onto continents. Consequently, it is difficult to constrain where and  
64 when intra-oceanic arcs resided throughout their life cycle, and tectonic reconstructions  
65 are often dominated by subduction systems close to continents [e.g. Müller and Landgrebe,  
66 2012]. Recently, studies mapping slab remnants imaged in seismic tomography [van der  
67 Meer et al., 2012; Domeier et al., 2017] point to the existence of previously unrecognized  
68 intra-oceanic subduction zones within the Pacific/Panthalassa domain that would have  
69 been active while Pangea was assembled or earlier in its dispersal, and much further from

70 the continents than more recent examples. This raises the question of how important the  
71 presence of continents is to the life cycle of subduction systems, and whether this influence  
72 varies between periods of supercontinent assembly and continental dispersal.

73 In this paper, we investigate the pattern of subduction initiation and cessation in time  
74 and space using numerical simulations of mantle convection. Numerical models are de-  
75 signed in a spherical annulus geometry, and we vary the number of continents, the strength  
76 of the lithosphere and its structure. We compare aspects of the modelling results to recon-  
77 structed subduction histories based on both plate kinematics and analysis of slab remnants  
78 imaged by seismic tomography [van der Meer et al., 2010, 2012; Müller et al., 2016]. We  
79 focus on global scale models to infer how the continental configuration and the plate layout  
80 change the distribution of subduction initiation and cessation, and the lifespan of subduc-  
81 tion zones. The models indicate that subduction initiation is non-randomly distributed  
82 in the ocean, and cessation happens mostly in the vicinity of continents. Our calculations  
83 point to different distributions of subduction inception between phases of supercontinents  
84 and phases in which continents are dispersed..

## 2. Method

85 In order to investigate statistically the spatial relationships between continents and the  
86 initiation, evolution and cessation of subduction zones, we numerically calculate the solu-  
87 tion of mantle convection in a spherical annulus [Hernlund and Tackley, 2008] using the  
88 StagYY code [Tackley, 2008]. The choice of geometry is motivated by the necessity of  
89 having long temporal series of several billions of years. Employment of the spherical annu-  
90 lus ensures similar scaling properties compared to the full 3D spherical shell. The model  
91 features self-consistently generated plate-like surface tectonics and drifting continents.

## 2.1. Physical and numerical model

We determine temperature, velocity, pressure and composition within the mantle by solving the equations of conservation of mass, momentum and energy and the advection of material composition considering an incompressible mantle under the Boussinesq approximation. Below, the equations are given in their dimensionless form.

$$\nabla \cdot \mathbf{v} = 0, \quad (1)$$

$$\nabla \cdot \left( \eta \left( \nabla \mathbf{v} + (\nabla \mathbf{v})^T \right) \right) - \nabla p = \text{Ra} (T + B C) \mathbf{e}_r, \quad (2)$$

$$\partial_t T + \mathbf{v} \cdot \nabla T = \nabla^2 T + H, \quad (3)$$

$$\partial_t C + \mathbf{v} \cdot \nabla C = 0, \quad (4)$$

with  $\mathbf{v}$  the velocity,  $p$  the static pressure,  $\eta$  the viscosity,  $T$  the temperature,  $C$  the composition,  $H$  the internal heating rate, Ra the Rayleigh number,  $B$  the buoyancy ratio and  $\mathbf{e}_r$  the radial unit vector.  $\partial_t$  is the partial time derivative.

Viscosity  $\eta$  follows the Arrhenius law and is strongly temperature and pressure dependent

$$\eta(T, p) = \eta_A \exp \left( \frac{E_a + p V_a}{RT} \right), \quad (5)$$

where  $E_a = 166 \text{ kJ mol}^{-1}$  is the activation energy (kept constant for all simulations),  $V_a = 6.34 \cdot 10^{-7} \text{ m}^3 \text{ mol}^{-1}$  the activation volume (constant for all simulations) and  $R = 8.314 \text{ J mol}^{-1} \text{ K}^{-1}$  the gas constant. We give all parameters in Table 1.  $\eta_A$  is set such that  $\eta$  matches the reference viscosity  $\eta_0$  at zero pressure and at temperature 1600 K, which is the expected temperature at the base of the lithosphere. We apply a viscosity cut off at  $10^4$  times  $\eta_0$ . The viscosity varies over 6 orders of magnitude over the temperature variation  $\Delta T$ , the superadiabatic temperature drop over the mantle. Independently of

116 temperature, viscosity increases exponentially by an order of magnitude with depth. The  
 117 lowest values of the viscosity are in the asthenospheric mantle, while at the core mantle  
 118 boundary viscosity is about 20 times lower than  $\eta_0$ .

119 To localize deformation in narrow zones and obtain realistic plate boundaries at the  
 120 surface, we use a pseudoplastic rheology [Moresi and Solomatov, 1998; Tackley, 2000a, b].  
 121 After reaching a certain threshold value, the yield stress  $\sigma_Y$ , the rocks undergo plastic  
 122 yielding.  $\sigma_Y$  is depth dependent and follows

$$123 \quad \sigma_Y = \sigma_0 + d \sigma'_Y, \quad (6)$$

124 where  $\sigma_0$  is the surface yield stress,  $d$  is the depth and  $\sigma'_Y$  is the yield stress depth  
 125 derivative. If the stress reaches  $\sigma_Y$ , we calculate the effective viscosity  $\eta_{\text{eff}}$  on the grid

$$126 \quad \eta_{\text{eff}} = \min [\eta(T, p), \eta_Y], \quad (7)$$

127 with  $\eta_Y$  as

$$128 \quad \eta_Y = \frac{\sigma_Y}{2\dot{\epsilon}_{\text{II}}}. \quad (8)$$

129  $\dot{\epsilon}_{\text{II}}$  is the second invariant of the strain rate tensor. We vary the surface strength  $\sigma_0$  of  
 130 the lithosphere between 7 MPa and 56 MPa while keeping the gradient constant for all  
 131 simulations at  $810 \text{ Pa m}^{-1}$ .

132 Using this kind of rheology results in the self-consistent formation of strong plate in-  
 133 teriors moving with a uniform velocity delimited by narrow plate boundaries character-  
 134 ized by reduced viscosity and an abrupt velocity change [Moresi and Solomatov, 1998;  
 135 Tackley, 2000b]. Importantly, such rheology successfully reproduces seafloor age dis-  
 136 tributions [Coltice et al., 2012] and is sufficiently realistic to investigate global surface  
 137 tectonics [Coltice et al., 2017; Ulvrova et al., 2019].



138 One of the important Earth-like features that is in general lacking in such convection  
139 models is single-sided subduction, i.e., subduction is often double-sided. This can be  
140 partially overcome by imposing a weak layer of oceanic oceanic crust at the surface, which  
141 gets advected into the subduction channel and hence decouples to a certain degree the  
142 sinking slab from the overriding plate, resulting in strong subduction asymmetry [Gerya  
143 et al., 2008; Crameri and Tackley, 2014]. In some of our simulations we include this weak  
144 crustal layer using tracers. The weak crustal layer is neutrally buoyant, and it follows the  
145 same viscosity law as ambient mantle but is characterized by a factor of 10 reduction in  $\eta_A$   
146 and it is more easily deformable (surface yield stress 18 MPa, yield gradient  $8.1 \text{ Pa m}^{-1}$ ).  
147 The initial thickness of the weak crustal layer is 20 km and it is converted to a regular  
148 mantle after reaching 290 km depth. In one case, we further improve the model and  
149 obtain one-sided subduction zones by imposing a free surface that can vertically deform.  
150 This is done using the so-called sticky-air method [Matsumoto and Tomoda, 1983] when  
151 vertical deformation of the mantle surface is allowed by prescribing an additional layer  
152 of "air" atop of the mantle. This layer is permanently forced to be isothermal (300 K),  
153 has close to zero density and very low viscosity, allowing it to be decoupled from the  
154 lithosphere. To obtain a valid solution, the air layer must be sufficiently thick while  
155 having low viscosity [Crameri et al., 2012]. We fix its initial thickness to 150 km and keep  
156 its viscosity at  $10^{-3}$  times  $\eta_0$ . This results in a high viscosity contrast between the plates  
157 at the surface and the air layer. The viscosity contrast is as high as  $10^7$ .

158 Continental rafts are modeled using the tracer-ratio method [Tackley and King, 2003].  
159 The detailed implementation is described elsewhere [Tackley and King, 2003; Rolf and  
160 Tackley, 2011]. We consider continents with an interior that is 300 km thick surrounded

161 by 140 km thick mobile belts in accordance with the thickness of the Archean cratons  
 162 and Proterozoic belts. Continents cover 30% of the model surface. In order to ensure the  
 163 stability of the continents, two conditions must be fulfilled: positive buoyancy and limited  
 164 deformation within continents [e.g. Doin et al., 1997; Lenardic and Moresi, 1999]. Based  
 165 on this, we choose a density contrast between continental material and ambient mantle  
 166 of  $-100 \text{ kg m}^{-3}$ , which gives the buoyancy ratio (ratio between the density contrast and  
 167 the thermal density variation) of -0.4. Furthermore, continents are  $100\times$  more viscous  
 168 than the ambient mantle and do not undergo pseudo-plastic deformation. Due to this  
 169 high rigidity, continental erosion by mantle flow is negligible and the rafts are stable over  
 170 billions of years.

171 The system is driven by heating from radioactive elements and from heat conducted  
 172 from the core. We keep the internal heating rate  $H$  constant at  $5.44 \times 10^{-12} \text{ W kg}^{-1}$   
 173 throughout the simulations. Core heat loss contributes around 20% to the total surface  
 174 heat flow, falling into the 10%–40% estimate for the Earth [Jaupart et al., 2015]. Both  
 175 the top and the bottom boundaries are isothermal and free-slip, except for the case with a  
 176 free deformable mantle surface, for which the top boundary of the computational domain  
 177 is no-slip above the air layer.

The convective vigour of the system is measured by the Rayleigh number  $\text{Ra}$

$$\text{Ra} = \frac{\rho_0 g \alpha \Delta T D^3}{\kappa \eta_0}, \quad (9)$$

178 where  $\rho_0$  is the reference density,  $g$  the gravitational acceleration,  $\alpha$  the thermal expan-  
 179 sivity,  $\Delta T$  is the superadiabatic temperature drop across the mantle with the thickness  
 180  $D$ ,  $\kappa$  is the thermal diffusivity and  $\eta_0$  is the reference viscosity. For all experiments, we  
 181 keep  $\text{Ra} = 10^6$  (calculated with  $\eta_0 = 6 \times 10^{22} \text{ Pa s}$ ). This is  $10 - 100\times$  lower than the

182 Earth's Rayleigh number, but lies at the edge of the computational feasibility for the  
183 given rheology and the presence of sticky air.

184 We use a resolution of  $128 \times 1024$  cells in the radial and horizontal directions, respec-  
185 tively, except for the case with the free surface when we use a grid with  $256 \times 2048$  cells.  
186 Vertical grid refinement close to the top and bottom limits is employed resulting in 10 km  
187 and 15 km (5 km and 8 km for the case with the sticky air) thick cells at the surface and  
188 at the core-mantle boundary (cf. more details in the supplementary material). To track  
189 composition, we use  $4 \times 10^7$  tracers. This means that on average there are around 300  
190 tracers per cell except in simulations with a free surface, which have higher resolution. In  
191 this case, the number of tracers per cell is around 75.

192 First, we run a model until it reaches a statistically steady state, at which the heat  
193 budget is balanced and characteristic properties of the system such as mean temperature,  
194 mean velocity and average surface heat flux fluctuate around some constant values. In this  
195 initial stage, we do not advect tracers and hence the composition field remains the same  
196 throughout the initialization period, which means that continents do not move from their  
197 initial positions. Once statistically steady state is achieved, we use a random snapshot  
198 from the equilibrated evolution to start the calculation with continents that move freely.  
199 The choice of the particular snapshot from the statistically steady state does not have any  
200 influence on the statistics performed on the system. The model is run until a sufficient  
201 number of subduction initiations  $N$  is collected. The shortest analyzed period is 1 Gy with  
202 27 subduction initiation events. The longest analyzed period is 7 Gy with 288 detected  
203 subduction initiations. The length of the simulation does not have any influence on the  
204 results as soon as  $N$  is large enough and statistically representative of the system. The

205 parameters of the calculations are listed in Table 1. We vary the strength of the oceanic  
206 lithosphere and number of continents, and we test how the presence of the weak crustal  
207 layer and presence of a free surface alter the results. In total, we run 13 models having  
208 different parameterizations.

## 2.2. Model analysis

209 To detect subduction inception and follow its evolution, we analyze the divergence of  
210 the surface velocity. As soon as a negative peak of the surface velocity divergence appears  
211 (the threshold of detection being minus one tenth of the surface rms velocity), a new  
212 subduction zone is formed. The motion of this peak is then tracked through time and we  
213 record the distance to the closest continental margin until the peak disappears. For each  
214 case we specifically register this distance at subduction inception and at cessation. These  
215 values are further analyzed by calculating a cumulative distribution of the distance to  
216 the closest continental margin specifically when subduction starts and ends. To construct  
217 these distributions we bin the range of all possible distances into 500 km wide intervals.  
218 We then count the cumulative number of detected distances falling into a specific bin.  
219 All subduction zones that initiate at a continental margin fall into the first bin. The  
220 long duration of each model allows us to collect up to several hundreds of subduction  
221 initiations, typically several tens of them.

222 To investigate systematic patterns within the distributions retrieved from the models,  
223 we use a Monte Carlo method and calculate the synthetic distribution for subduction  
224 zones initiating at random positions within oceans. At each model time we generate a set  
225 of randomly located points within the oceans, which together we take to have a spatial  
226 distribution equivalent to scenarios where subduction initiation or cessation locations

227 is also randomly distributed. For models with one continent, the cumulative frequency  
228 of random point locations as a function of distance to the continent is a straight line  
229 since the distance between the two continental margins is constant through time and the  
230 probability that a subduction zone initiates at a certain location is uniform. For more  
231 than one continent, the distribution is typically curved. This allows us to show how the  
232 modelled subduction distributions deviate from the random one. However, it is necessary  
233 that a sufficiently large number of random subduction initiations is generated at each  
234 time level, in total at least several thousand. To estimate the variance of the random  
235 distribution, we calculate distributions of  $N$  subduction initiation events that happen  
236 at random times and random positions.  $N$  is the number of initiations detected in the  
237 particular model.

### 3. Results

238 The organization of the system dictates its dynamic evolution: sinking slabs drive  
239 plate motion while inducing the mantle flow that in turn is at the origin of the plate  
240 motion (Figure 1). Plate-like behaviour is developed self-consistently using the yielding  
241 rheology (cf. Section 2.2) with a surface velocity that is constant in plate interiors while  
242 changing abruptly over plate boundaries. Since the system is heated mainly by internal  
243 heat sources (and we keep the internal heating rate constant for all simulations), sinking  
244 slabs and surface plates that compose the upper boundary layer dominate over plumes  
245 created at the core-mantle boundary. In particular, around 20% of the total surface heat  
246 flux is due to heating the mantle from the core. . The core derived fraction of the  
247 total surface heat flux is very similar for all models, with differences smaller than 1%.  
248 When looking at the temperature structure of the system (Figure 1b,e,h), one can note

249 that there is a strong subadiabatic gradient (Figure 1c,f,i). This is partly because the  
250 system is internally heated but more importantly negative gradients arise due to pressure  
251 dependent viscosity [Christensen, 1985].

252 Subduction zones (and in this study we refer to subduction zones as convective down-  
253 welling currents in the numerical simulations) next to continental margins are one-sided  
254 while a distinctive asymmetry is observed for intra-oceanic subduction zones (cf. Figure 1  
255 and animation S1 in the supporting material). The degree of asymmetry in the latter case  
256 changes through time and differs among models. The dip angle with which plates sink into  
257 the mantle is generally large (close to vertical, Figure 1a) but more realistic behaviour is  
258 observed (i.e. shallower dip angles) in models with the weak crustal layer that allows par-  
259 tial decoupling between the sinking and overriding plates (Figure 1d), or in models with  
260 a free surface (Figure 1g). However, these models are still far from producing Earth-like  
261 subduction zones in their entirety, with modeled sinking plates commonly experiencing  
262 phases of symmetrical subduction during their lifespans, for example at their inception  
263 or during polarity flips (Figure 2). Cramer and Tackley [2014] have observed polarity  
264 reversals for intra-oceanic subduction in models with a similar parameterization but in  
265 3D. Our models also show polarity reversals at the continent-ocean boundary (Figure 2).

### 3.1. Influence of lithospheric strength

266 To investigate the impact of the lithospheric strength on subduction initiation we run  
267 several models with different yield stress  $\sigma_0$ , which we vary between 7 and 56 MPa. The  
268 plate size hence number of subduction zones is strongly influenced by how difficult it  
269 is for the lithosphere to localize deformation, which is directly related to the value of  
270  $\sigma_0$ . Decreasing the surface yield stress results in weaker oceanic lithosphere and smaller

271 plates [Moresi and Solomatov, 1998; Tackley, 2000b; Coltice et al., 2017; Langemeyer  
272 et al., 2018]. For low yield stress ( $\sigma_0 = 7$  MPa), a large population of subduction zones  
273 exists at a given instant, fluctuating around 7 and 8 (cf. histogram on Figure 3a). The  
274 distribution of subduction initiation within the oceans can be characterized as a random  
275 process distribution as it follows the distribution of subduction zones that are randomly  
276 initiated in within oceans (Figure 3a). There are small deviations of the distribution  
277 from the mean synthetic random distribution, which fall into the variance of the random  
278 distribution. This is due to finite number of subduction zones collected for this model  
279 ( $N = 89$ ). The fact that these deviations are small indicates that the number of subduc-  
280 tion zones collected is sufficient. The number of subduction zones that are formed in the  
281 vicinity of a continental margin (closer than 500 km) is small, around 5% (Figure 3a). A  
282 stiffer lithosphere ( $\sigma_0 = 35$  MPa, Figure 3b) promotes subduction initiation proximal to  
283 continents, with around 30% of subduction zones being formed close to continental mar-  
284 gins. Within this case, the influence of the continents on subduction initiation is strongest  
285 close to the continents, which is in accordance with previous studies that showed stress  
286 focusing at the continental margins [Rolf and Tackley, 2011]. Beyond a certain threshold  
287 distance from the continents the probability of subduction initiation is essentially random.  
288 For intermediate yield stress ( $\sigma_0 = 35$  MPa) this distance is around 3000 km (Figure 3b).  
289 For very stiff lithosphere ( $\sigma_0 = 56$  MPa), the distance within which continents influence  
290 the stress distribution becomes greater still, with no clear threshold between random and  
291 controlled behaviour (Figure 3c). The frequency of subduction initiation in the immediate  
292 proximity of continental margins is further increased and is close to 40% for strong oceans  
293 with few (around two) subduction zones on average (Figure 3c and Figure 4a).

294 Subduction zones that are formed next to a continental margin stay glued to the con-  
295 tinent their whole existence (Figure 5). In contrast, subduction zones that initiate as  
296 intra-oceanic reside in the oceans where they either merge with another subduction zone  
297 or migrate in the oceans before reaching a continental margin where they endure for some  
298 time before ceasing (Figure 5). In some cases, a subduction zone retreats toward the con-  
299 tinent and once it hits the margin, subduction continues with a reversed polarity (Figure  
300 2). Rarely, a subduction zone is formed and ceases as intra-oceanic without colliding with  
301 another convergence zone (Figure 5). In the weak lithosphere case, termination is random  
302 just like initiation (Figure 3a). Where the continents have an influence, subduction zones  
303 are more likely to terminate adjacent to continents than to initiate there, which is pre-  
304 sumably a consequence of intra-oceanic subduction zones being able to migrate freely, but  
305 once they migrate to a continental margin subduction zones stay there until they cease  
306 (Figure 3b and c).

### 3.2. Influence of number of continental margins

307 Repeated continental assembly and dispersal are observed on Earth in the cycles that  
308 last for several 100 Myr [e.g. Rogers and Santosh, 2004]. The length of the continen-  
309 tal margins thus varies according to the continental configuration, being minimal when  
310 continents are aggregated and maximal when dispersed. To investigate the influence of  
311 the number of continental margins on the position of subduction initiation within our  
312 annulus models, we perform a set of calculations with one, two and three continental rafts  
313 (where each raft has two margins), while keeping the total cover of continents constant at  
314 30% of the annulus. The number of continental margins in 2D models corresponds to the  
315 length of the continental margins in 3D. In these models, we keep the yield stress fixed



316 ( $\sigma_0 = 35$  MPa) and include a weak crustal layer at the surface. The number of subduction  
317 zones fluctuates around four or five (cf. histograms on Figure 6). With increasing num-  
318 ber of continental margins, the number of intra-oceanic subduction initiations decreases,  
319 regardless of whether a weak crustal layer is present (cf. Figure 4b). In particular, subduc-  
320 tion initiation at continental margins increases from 30% for the case with one continent  
321 to 67% for three continents (cf. Figure 4b and 6). Two fundamental results are consistent  
322 across all model cases: firstly, all cases significantly differ from initiation at random po-  
323 sition for the chosen lithospheric strength; secondly, we systematically observe that more  
324 subduction zones cease at a continental margin compared to the initiation position (cf.  
325 Figure 6). Both these relationships are weakest for the case with a single continent (cf.  
326 Figure 6a). The threshold distance below which the effect of continents is negligible and  
327 the distribution follows a random distribution of subduction initiation increases with in-  
328 creasing number of continental margins and is around 4000 km, 6000 km and 7000 km for  
329 cases with two, four and six continental margins (Figure 6).

### 3.3. Asymmetric subduction zones

330 At the surface of the Earth, during a collision of two oceanic plates, one of them subducts  
331 into the mantle while the overriding plate stays at the surface. Although numerical mod-  
332 els still have limited ability to produce such behavior, strong asymmetry of sinking slabs  
333 is observed in our models as is described in the beginning of this section. The simplest  
334 model, with a free-slip surface and no weak crustal layer features the least realistic sub-  
335 duction dipping angles and longer periods of vertical descent. In this case, about 45% of  
336 subduction inceptions are adjacent to the continental margins (Figure 7a). For more com-  
337 plex models with more realistic slab dip angles due to lubrication and partial decoupling

338 at the interface between the two colliding plates (models with the weak crustal layer), it is  
339 more likely that subduction initiates at the continental margin; close to 60% of detected  
340 subduction zones start in the vicinity of the continent (Figure 7b). This is because the  
341 lateral density gradient between continental and oceanic lithosphere produces additional  
342 compressive stresses that would drive continents to spread below the free-slip boundary,  
343 if the viscosity was low enough. Hence compressive stresses focus at the continent ocean  
344 boundary [Nikolaeva et al., 2010; Rolf and Tackley, 2011] and favour subduction initiation.  
345 In combination with a weak crustal layer having lower yield stress and hence localizing  
346 deformation more easily, more subduction zones initiate at the continental margins. For  
347 the models with a free, deformable surface that features more realistic slab dips and stress  
348 states, the number of initiation events at the continental margins drops to around 30%  
349 (Figure 7c). In this case, the free surface allows the continent to hamper continent spread-  
350 ing by generating a topography that can accommodate a fraction of the stresses at the  
351 continent ocean boundary and the lateral density difference between the continents and  
352 the mantle through isostasy.

### 3.4. Reconstructions of subduction, initiation, and cessation

353 The timing and location of past subduction can be reconstructed from geological and  
354 geophysical constraints, though such reconstructions are subject to large uncertainties  
355 over the timescales of supercontinent cycles (several hundred Myr). In particular, the  
356 lengths and locations of plate boundaries within the oceanic realm far from continents  
357 are poorly known, increasingly so further back in time, since the crust that comprised  
358 these regions is scarcely preserved at the present day. We compare two reconstructions  
359 of subduction history (Figure 8) that are derived by different methods, and use these as

360 points of comparison with numerical model behaviour. The first reconstruction maps the  
361 extent of subduction zones within a globally self-consistent framework of plate boundary  
362 configurations and plate kinematics [Müller et al., 2016]; the second reconstruction uses  
363 subducted slab signatures mapped within seismic tomography models as the primary line  
364 of evidence [van der Meer et al., 2010, 2012]. Both reconstructions attempt to reconcile  
365 geologic observations from arc remnants to some extent, but nonetheless differ in many  
366 aspects - notably, slab remnants interpreted from seismic tomography suggest a much  
367 larger population of intra-oceanic subduction zones. Qualitatively, subduction zones in  
368 the Müller et al. [2016] reconstruction are typically closer to the continents compared to  
369 those in the interpretation of van der Meer et al. [2010, 2012] (Figure 8). Below we describe  
370 a first-order quantification of the proximity to continents of subducting segments and their  
371 initiation and cessation in both reconstructions, which offers some degree of comparison  
372 with the results of the numerical simulations described in Section 2.2. The supporting  
373 material contains the computer code and data files used to perform this analysis and a  
374 detailed explanation of the steps we followed.

375 In computing distributions functions for reconstructions, uncertainty arises when we  
376 attempt to measure the distance from individual segments along a subduction zone to the  
377 nearest continent - such measurements require a clear definition of what does and does  
378 not constitute a continent within the reconstructions. The distinction is not clear-cut for  
379 the Earth, which contains a spectrum of stretched, submerged continental fragments that  
380 have not conventionally been considered continents [e.g. Mortimer et al., 2017], and where  
381 the nature of the crust in the overriding plate can change significantly along strike for  
382 individual arcs (for example the present-day Aleutian arc). Using a set of reconstructable

383 polygons defining major continental blocks (Figure 8, see also supporting information)  
384 we first derived the curves in Figure 9 by generating sets of randomly distributed points  
385 within the oceans at different reconstruction times. We then compute the distance of each  
386 point to the nearest continent boundary, and plot the cumulative distribution functions  
387 of these distances subdivided into 25 Myr time windows. These results provide a visual  
388 baseline to show how the distances to the continents of subduction segments compare to  
389 the pattern expected from a random process, similar to that used in Figures 3, 6 and 7  
390 but on a spherical Earth rather than an annulus.

391 For the Müller et al. [2016] reconstruction, we extract subduction zone geometries at 1  
392 Myr intervals and resample each line geometry to uniformly spaced half-degree segments.  
393 We compute the distance of segment mid-points to the nearest continent boundary, such  
394 that the distances that contribute to the cumulative distributions may vary significantly  
395 along each distinct line feature. These distances are illustrated for each reconstruction  
396 time in animation S2, and form the basis of the cumulative distribution functions in  
397 Figure 9b where the results are subdivided into 25 Myr time bins. Subduction initiation  
398 and termination is not explicitly encoded into the kinematic reconstruction, and so we  
399 used simple criteria to detect initiating and ceasing segments. The main criterion is that  
400 initiating or ceasing segments will not lie within a threshold distance of any segment from  
401 the network of subduction zones from 1 Myr earlier or later. The threshold is required  
402 because trenches where subduction is ongoing will migrate by a finite amount over 1 Myr  
403 (animation S2), and we use a threshold distance of 200 km to allow for the magnitude  
404 of trench migration expected within 1 Myr [Williams et al., 2015]. An exception to this  
405 criterion is segments that lie within this threshold distance, but where the pair of plates

406 that bound the adjacent segments differs between successive plate boundary snapshots 1  
407 Myr apart (occurring for example in cases of reconstructed subduction polarity reversal,  
408 which we consider as termination of existing subduction and initiation of a new segment).  
409 Locations of subduction initiation and cessation defined in this way are highlighted in  
410 animation S2, and the distances to the nearest continents at these points form the basis  
411 of the cumulative distribution functions in Figure 9c.

412 For subduction history interpreted from seismic tomography, we compute the distance  
413 to the nearest continent of the line geometries defined by these previous studies at discrete  
414 reconstruction times being 7 to 17 Myr apart. We make an important distinction between  
415 slabs tabulated in van der Meer et al. [2010] (Figure 9e) and the longer list of slabs  
416 considered in van der Meer et al. [2012] (Figure 9d). For the former, the top and bottom  
417 slab ages are available and we take them as the timings of subduction termination and  
418 initiation respectively. The histories of additional slabs mapped in van der Meer et al.  
419 [2012] are not defined with the same level of detail. Consequently we do not include  
420 pre-Cenozoic subduction interpreted from slab remnants beneath the Pacific in two of our  
421 distribution plots (Figure 9e,f).

422 With these limitations in mind, we ask the question as to whether the patterns of sub-  
423 duction initiation and cessation contained within current reconstructions follow a similar  
424 distribution to that observed in our numerical models. The distribution of subduction  
425 in relation to continents from the alternative subduction histories is illustrated using cu-  
426 mulative distribution functions (Figure 9), providing some analogy to the annulus model  
427 results. For both subduction histories, the overall distribution of ongoing subduction is  
428 typically closer to the continents than expected for randomly distributed points within

429 the oceans (Figure 9b,d,e). This pattern is particularly pronounced for the Müller et al.  
430 [2016] kinematic reconstruction (Figure 9b), which lacks many intra-oceanic systems in-  
431 terpreted by van der Meer et al. [2010, 2012] from seismic tomography. When we isolate  
432 subduction initiation and cessation (Figure 9c,f), a further trend emerges that is apparent  
433 in both kinematic and tomography-based subduction histories - subduction cessation is  
434 typically closer to the continents than subduction initiation. This trend is only absent in  
435 the poorly resolved pre-100 Ma section of the Müller et al. [2016] reconstruction and the  
436 results do not show an obvious distinction between the periods before and after 100 Ma,  
437 broadly corresponding to the periods of initial and later stages of dispersal of Pangea.  
438 However, since the distributions for tomography-based initiation and termination do not  
439 include additional slabs interpreted to have existed within the middle of the Panthalassic  
440 ocean (Figure 8), the proportion of cases far from continents while Pangea was assembled  
441 are likely to be underestimated in our plots.

#### 4. Discussion

442 Previous studies into the effect of continents on mantle dynamics have shown that con-  
443 tinents increase the wavelength of the convective flow [e.g. Guillou and Jaupart, 1995] and  
444 influence heat loss out of the system as they act as thermal insulators [e.g. Lenardic and  
445 Moresi, 1999; Rolf et al., 2012]. Importantly, numerical simulations and laboratory exper-  
446 iments suggest that continents change the lithospheric stress distribution and facilitate  
447 subduction initiation [e.g. Nikolaeva et al., 2010; Rolf and Tackley, 2011]. However, sys-  
448 tematic study of the locations of subduction initiation and their ensuing evolution taking  
449 into account global tectonic settings has received very little attention.

450 Comparison between the distribution of subduction in numerical simulations and those  
451 inferred from reconstructions offers insight into the most plausible model parameters.  
452 Models in which the lithospheric strength is low, such that subduction is effectively ran-  
453 domly distributed within the oceans, are inconsistent with the inferred patterns of sub-  
454 duction on Earth during the last >200 Myr (Figure 9). Instead, the distributions from  
455 reconstructions are more compatible with scenarios in which the lithospheric strength is  
456 relatively high, such that the continents generate a strain shadow promoting subduction  
457 initiation closer to the continents. This region adjacent to margins is loaded by the den-  
458 sity and topography contrast between continent and ocean lithosphere. Therefore, the  
459 lithosphere more readily yields upon experiencing additional stresses produced by convec-  
460 tion, whereas the same convective stresses alone are less likely to reach the yield criterion  
461 further from continents.

462 In models where sites of initiation of subduction are biased towards regions close to  
463 continents, the distribution of subduction throughout its duration and cessation is also  
464 naturally biased towards these regions. Subduction that initiates at a continental margin  
465 remains there until it ceases. Subduction systems initiating in the oceans may migrate  
466 towards or away from the nearby continental margins; those that reach the continent mar-  
467 gin become continental arcs, and remain so until subduction ceases. Hence, the control  
468 of continents on patterns of subduction initiation influences the distribution of subduc-  
469 tion cessation, such that subduction termination along continental margins occurs more  
470 frequently than subduction initiation, even in the absence of continent-continent collision.

471 Comparison between models with different numbers of continents (and therefore mar-  
472 gins) offers an insight into the different distributions of subduction that we may expect

473 during different phases of the supercontinent cycle. Cases with two or three distinct con-  
474 tinents (analogous to periods of continental dispersal such as the last  $\sim 100$  Myr on Earth)  
475 are more favorable to subduction initiation close to continental margins - in contrast, when  
476 the annulus includes only one continent (analogous to a supercontinent such as Pangea),  
477 the area influenced by the continental strain shadow effect is reduced and the proportion  
478 of subduction initiations (and terminations) occurring within the oceans increases. This  
479 result contrasts with the results for the Müller et al. [2016] kinematic reconstruction,  
480 where very little subduction initiates, evolves, or ceases far from continents prior to 100  
481 Ma (Figure 9b,c). However, distributions from kinematic reconstructions also contrast  
482 with those for alternative subduction histories interpreted from seismic tomography - in  
483 particular when these take into account Triassic-Jurassic, intra-Panthalassa subduction  
484 systems of van der Meer et al. [2012], illustrated in Figure 8 and included in the distri-  
485 bution of Figure 9d but not included in Figure 9f. The ages and locations of subduction  
486 initiation for these systems is unknown, but it is reasonable to infer that some or all of  
487 these systems initiated far from Pangea.

488 In addition to the global studies of van der Meer et al. [2010] and van der Meer et al.  
489 [2012], regional studies have also interpreted tomography to reveal previously unrecog-  
490 nised intra-oceanic subduction zones existing within Panthalassa during the Cretaceous  
491 and earlier [Domeier et al., 2017; Sigloch and Mihalynuk, 2013]. Furthermore, numerical  
492 models of past mantle flow constrained by subduction histories similar to that of Müller  
493 et al. [2016] produce present-day temperature fields that show good agreement with deep  
494 mantle seismic velocity variations imaged by tomography to first-order [Flament et al.,  
495 2017] but yield regional mismatches around parts of the Pacific which may be resolved



496 when additional intra-oceanic subduction zones are incorporated [e.g. Braz et al., 2018].  
497 The emerging view from observations is that intra-oceanic subduction was more preva-  
498 lent during Pangea’s existence and early breakup than previously recognised. Our model  
499 results in which intra-oceanic subduction initiation and evolution is favoured during su-  
500 percontinental assembly are consistent with this view, even though our models lack many  
501 features of real-world plate tectonics. Even during supercontinent assembly we would still  
502 expect a greater likelihood of intra-oceanic subduction initiation proximal to continental  
503 margins in the geological record [e.g. Maffione et al., 2017].

504 One must keep in mind that numerical simulations have certain limitations. Primarily,  
505 the study relies on 2D calculations, in which only poloidal flow can exist. We do not  
506 consider any 3D characteristics of mantle flow such as toroidal motion around lateral slab  
507 edges that can slow down descending slabs [Li and Ribe, 2012]. The models operate at  
508 a Rayleigh number that is lower than the Earth’s and hence result in thicker boundary  
509 layers, less vigorous convection and surface heat flow and plate velocities lower than what  
510 is expected for our planet. Although basal heating in the models (representing around  
511 20% of the total surface heat flux) falls into the estimated range of the Earth’s basal  
512 heat flux portion [Jaupart et al., 2015], we fix the internal heating rate and we possibly  
513 underestimate the influence of plumes. Subduction can be initiated when plumes provide  
514 sufficient additional stresses causing local weakening of the lithosphere after hitting the  
515 subsurface [Gerya et al., 2008]. However, this is not our case since the plumes in the  
516 models are relatively weak and hence only rarely trigger the formation of new convergent  
517 boundaries. Importantly, the employed rheology neglects any past deformation of the  
518 lithosphere and reflects only the instantaneous stress distribution. However, on Earth

519 plates have memory of previous yielding and can be damaged or undergo healing [e.g  
520 Bercovici and Ricard, 2016].

## 5. Conclusions

521 We present an assessment of where subduction initiates and ceases in global convec-  
522 tion models with a plate-like surface and continental drift. We compare the results of  
523 numerical simulations with distributions of subduction initiation and cessation retrieved  
524 from plate tectonics reconstructions and seismic tomography models. We show that the  
525 location of subduction initiation and cessation is not randomly distributed within the  
526 oceans on Earth. Subduction zones that are formed at continental margins tend to stay  
527 there, while subduction zones formed within the oceans migrate and merge with other  
528 intra-oceanic subduction zones, or reach continental margins where subduction usually  
529 continues, changing polarity before eventually ceasing. Hence, we systematically find  
530 that more subduction zones cease in the vicinity of continental margins compared to sub-  
531 duction initiation. Numerical models indicate that the critical parameters that influence  
532 the position of subduction initiation are the lithospheric strength and the number of con-  
533 tinental margins. Stronger lithosphere (which implies larger plates and fewer subduction  
534 zones [Tackley, 2000b]) increases the probability of subduction initiation in the vicinity of  
535 continental margins. With our numerical simulations we also predict that intra-oceanic  
536 subduction initiation is more likely during the times of supercontinent assembly, while  
537 continental dispersal favors incipient subduction close to continents. These results favour  
538 interpretations of intra-oceanic subduction systems within the Panthalassa Ocean during  
539 the time of Pangea based on seismic tomography [van der Meer et al., 2012; Van Der Meer  
540 et al., 2014], which are missing from earlier plate tectonic reconstructions.

541 **Acknowledgments.** The support for this research has been provided by the Eu-  
542 ropean Union’s Horizon 2020 research and innovation program under the ERC grant  
543 agreement n°617588 and the Marie Skłodowska Curie grant agreement n°753755.  
544 Simulations were performed on the AUGURY super-computer at P2CHPD Lyon.  
545 The StagPy library was used in this study to process StagYY output data  
546 (<https://github.com/StagPython/StagPy>). The pygplates library was used to anal-  
547 yse plate tectonic reconstructions (<https://www.gplates.org/docs/pygplates/>).

## References

- 548 Auzende, J.M., Lafoy, Y., Marsset, B., 1988. Recent geodynamic evolution of the north  
549 Fiji basin (southwest Pacific). *Geology* 16, 925–929.
- 550 Baes, M., Sobolev, S.V., Quinteros, J., 2018. Subduction initiation in mid-ocean induced  
551 by mantle suction flow. *Geophys. J. Int.* 215, 1515–1522.
- 552 Bercovici, D., Ricard, Y., 2016. Grain-damage hysteresis and plate tectonic states. *Phys.*  
553 *Earth Planet. Inter.* 253, 31 – 47.
- 554 Braz, C., Seton, M., Flament, N., Müller, R.D., 2018. Geodynamic reconstruction of an  
555 accreted cretaceous back-arc basin in the northern andes. *Journal of Geodynamics* 121,  
556 115–132.
- 557 Christensen, U.R., 1985. Heat transport by variable viscosity convection ii: pressure  
558 influence, non-newtonian rheology and decaying heat sources. *Physics of the Earth and*  
559 *Planetary Interiors* 37, 183 – 205.
- 560 Coltice, N., Gérard, M., Ulvrova, M., 2017. A mantle convection perspective on global  
561 tectonics. *Earth-Sci. Rev.* 165, 120 – 150.

- 562 Coltice, N., Rolf, T., Tackley, P.J., Labrosse, S., 2012. Dynamic causes of the relation  
563 between area and age of the ocean floor. *Science* 336, 335–338.
- 564 Cramer, F., Schmeling, H., Golabek, G.J., Duretz, T., Orendt, R., Buitter, S.J.H., May,  
565 D.A., Kaus, B.J.P., Gerya, T.V., Tackley, P.J., 2012. A comparison of numerical sur-  
566 face topography calculations in geodynamic modelling: an evaluation of the sticky air  
567 method. *Geophys. J. Int.* 189, 38–54.
- 568 Cramer, F., Tackley, P.J., 2014. Spontaneous development of arcuate single-sided sub-  
569 duction in global 3-D mantle convection models with a free surface. *J. Geophys. Res.:*  
570 *Solid Earth* 119, 5921–5942.
- 571 Dilek, Y., Furnes, H., 2009. Structure and geochemistry of tethyan ophiolites and their  
572 petrogenesis in subduction rollback systems. *Lithos* 113, 1–20.
- 573 Doin, M.P., Fleitout, L., Christensen, U., 1997. Mantle convection and stability of depleted  
574 and undepleted continental lithosphere. *J. Geophys. Res.:* *Solid Earth* 102, 2771–2787.
- 575 Domeier, M., Shephard, G.E., Jakob, J., Gaina, C., Doubrovine, P.V., Torsvik, T.H.,  
576 2017. Intraoceanic subduction spanned the Pacific in the Late Cretaceous–Paleocene.  
577 *Science Advances* 3, eaao2303.
- 578 Flament, N., Williams, S., Müller, R., Gurnis, M., Bower, D.J., 2017. Origin and evolution  
579 of the deep thermochemical structure beneath eurasia. *Nature communications* 8, 14164.
- 580 Gerya, T., Stern, R., Baes, M., Sobolev, S., Whattam, S., 2015. Plate tectonics on the  
581 earth triggered by plume-induced subduction initiation. *Nature* 527, 221–225.
- 582 Gerya, T.V., Connolly, J.A., Yuen, D.A., 2008. Why is terrestrial subduction one-sided?  
583 *Geology* 36, 43–46.

- 584 Guillou, L., Jaupart, C., 1995. On the effect of continents on mantle convection. *J.*  
585 *Geophys. Res.: Solid Earth* 100, 24217–24238.
- 586 Hegarty, K.A., Weissel, J.K., Hayes, D.E., 1982. Convergence at the Caroline-Pacific Plate  
587 Boundary: Collision and Subduction. American Geophysical Union. pp. 326–348.
- 588 Hernlund, J.W., Tackley, P.J., 2008. Modeling mantle convection in the spherical annulus.  
589 *Phys. Earth Planet. Inter.* 171, 48–54.
- 590 Jaupart, C., Labrosse, S., Lucazeau, F., Mareschal, J., 2015. 7.06 - temperatures, heat  
591 and energy in the mantle of the earth, in: Schubert, G. (Ed.), *Treatise on Geophysics*  
592 (Second Edition). Elsevier, Oxford. volume 7, Second edition edition. pp. 223–270.
- 593 Kerrick, D.M., 2001. Present and past nonanthropogenic co<sub>2</sub> degassing from the solid  
594 earth. *Reviews of Geophysics* 39, 565–585.
- 595 Langemeyer, S.M., Lowman, J.P., Tackley, P.J., 2018. The sensitivity of core heat flux to  
596 the modeling of plate-like surface motion. *Geochem., Geophys., Geosyst.* 19, 1282–1308.
- 597 Lebrun, J.F., Lamarche, G., Collot, J.Y., 2003. Subduction initiation at a strike-slip  
598 plate boundary: The cenozoic pacific-australian plate boundary, south of new zealand.  
599 *Journal of Geophysical Research: Solid Earth* 108.
- 600 Lee, S.M., 2004. Deformation from the convergence of oceanic lithosphere into Yap trench  
601 and its implications for early-stage subduction. *J. Geodynamics* 37, 83 – 102.
- 602 Lenardic, A., Moresi, L.N., 1999. Some thoughts on the stability of cratonic lithosphere:  
603 Effects of buoyancy and viscosity. *J. Geophys. Res.: Solid Earth* 104, 12.
- 604 Leng, W., Gurnis, M., 2015. Subduction initiation at relic arcs. *Geophys. Res. Lett.* 42,  
605 7014–7021.

- 606 Li, Z.H., Ribe, N.M., 2012. Dynamics of free subduction from 3-d boundary element  
607 modeling. *Journal of Geophysical Research: Solid Earth* 117.
- 608 Lowman, J.P., 2011. Mantle convection models featuring plate tectonic behavior: An  
609 overview of methods and progress. *Tectonophys.* 510, 1–16.
- 610 Maffione, M., van Hinsbergen, D.J., de Gelder, G.I., van der Goes, F.C., Morris, A.,  
611 2017. Kinematics of Late Cretaceous subduction initiation in the neo-tethys ocean  
612 reconstructed from ophiolites of Turkey, Cyprus, and Syria. *J. Geophys. Res.: Solid*  
613 *Earth* 122, 3953–3976.
- 614 Matsumoto, T., Tomoda, Y., 1983. Numerical simulation of the initiation of subduction  
615 at the fracture zone. *Journal of Physics of the Earth* 31, 183–194.
- 616 van der Meer, D.G., Spakman, W., Van Hinsbergen, D.J., Amaru, M.L., Torsvik, T.H.,  
617 2010. Towards absolute plate motions constrained by lower-mantle slab remnants. *Nat.*  
618 *Geosci.* 3, 36–40.
- 619 van der Meer, D.G., Torsvik, T.H., Spakman, W., Van Hinsbergen, D.J.J., Amaru, M.L.,  
620 2012. Intra-panthalassa ocean subduction zones revealed by fossil arcs and mantle  
621 structure. *Nat. Geosci.* 5, 215–219.
- 622 Michaud, F., Royer, J.Y., Bourgois, J., Dymant, J., Calmus, T., Bandy, W., Sosson, M.,  
623 Mortera-Gutiérrez, C., Sichel, B., Rebolledo-Viera, M., et al., 2006. Oceanic-ridge  
624 subduction vs. slab break off: Plate tectonic evolution along the baja california sur  
625 continental margin since 15 ma. *Geology* 34, 13–16.
- 626 Moresi, L., Solomatov, V., 1998. Mantle convection with a brittle lithosphere: thoughts  
627 on the global tectonic styles of the earth and venus. *Geophys. J. Int.* 133, 669–682.

- 628 Mortimer, N., Campbell, H.J., Tulloch, A.J., King, P.R., Stagpoole, V.M., Wood, R.A.,  
629 Rattenbury, M.S., Sutherland, R., Adams, C.J., Collot, J., et al., 2017. Zealandia:  
630 Earths hidden continent. *GSA Today* 27, 27–35.
- 631 Müller, R., Landgrebe, T., 2012. The link between great earthquakes and the subduction  
632 of oceanic fracture zones. *Solid Earth* 3, 447–465.
- 633 Müller, R.D., Seton, M., Zahirovic, S., Williams, S.E., Matthews, K.J., Wright, N.M.,  
634 Shephard, G.E., Maloney, K.T., Barnett-Moore, N., Hosseinpour, M., Bower, D.J.,  
635 Cannon, J., 2016. Ocean Basin Evolution and Global-Scale Plate Reorganization Events  
636 Since Pangea Breakup. *Ann. Rev. Earth Planet. Sci.* 44, 107–138.
- 637 Nikolaeva, K., Gerya, T.V., Marques, F.O., 2010. Subduction initiation at passive mar-  
638 gins: Numerical modeling. *J. Geophys. Res.: Solid Earth* 115, B03406.
- 639 Reagan, M.K., Ishizuka, O., Stern, R.J., Kelley, K.A., Ohara, Y., Blichert-Toft, J.,  
640 Bloomer, S.H., Cash, J., Fryer, P., Hanan, B.B., et al., 2010. Fore-arc basalts and  
641 subduction initiation in the izu-bonin-mariana system. *Geochem., Geophys., Geosyst.*  
642 11.
- 643 Rogers, J., Santosh, M., 2004. *Continents and Supercontinents*. Oxford University Press.
- 644 Rolf, T., Coltice, N., Tackley, P., 2012. Linking continental drift, plate tectonics and the  
645 thermal state of the Earth’s mantle. *Earth Planet. Sci. Lett.* 351, 134–146.
- 646 Rolf, T., Tackley, P., 2011. Focussing of stress by continents in 3D spherical mantle  
647 convection with self-consistent plate tectonics. *Geophys. Res. Lett.* 38.
- 648 Sigloch, K., Mihalynuk, M.G., 2013. Intra-oceanic subduction shaped the assembly of  
649 cordilleran north america. *Nature* 496, 50.

- 650 Stern, R.J., 2004. Subduction initiation: spontaneous and induced. *Earth Planet. Sci.*  
651 *Lett.* 226, 275–292.
- 652 Tackley, P.J., 2000a. The Quest for Self-Consistent Generation of Plate Tectonics in  
653 Mantle Convection Models. American Geophysical Union, Washington, D.C.. volume  
654 121 of *Geophys. Monograph.* pp. 47–72.
- 655 Tackley, P.J., 2000b. Self-consistent generation of tectonic plates in time-dependent,  
656 three-dimensional mantle convection simulations 1. pseudoplastic yielding. *Geochem.,*  
657 *Geophys., Geosyst.* 1.
- 658 Tackley, P.J., 2008. Modelling compressible mantle convection with large viscosity con-  
659 trasts in a three-dimensional spherical shell using the yin-yang grid. *Phys. Earth Planet.*  
660 *Inter.* 171, 7–18.
- 661 Tackley, P.J., King, S.D., 2003. Testing the tracer ratio method for modeling active  
662 compositional fields in mantle convection simulations. *Geochem., Geophys., Geosyst.*  
663 4, 8302.
- 664 Ulvrova, M.M., Brune, S., Williams, S., 2019. Breakup without borders: How continents  
665 speed up and slow down during rifting. *Geophysical Research Letters* 46, 1338–1347.
- 666 Van Der Meer, D.G., Zeebe, R.E., van Hinsbergen, D.J., Sluijs, A., Spakman, W., Torsvik,  
667 T.H., 2014. Plate tectonic controls on atmospheric co2 levels since the triassic. *Proc.*  
668 *Nat. Acad. Sci.* 111, 4380–4385.
- 669 Williams, S., Flament, N., Müller, R.D., Butterworth, N., 2015. Absolute plate motions  
670 since 130 ma constrained by subduction zone kinematics. *Earth and Planetary Science*  
671 *Letters* 418, 66–77.



<i>Variable</i>	<i>Symbol</i>	<i>Nondimensional Value</i>	<i>Dimensional Value</i>
Gravitational acceleration	$g$	-	$9.81 \text{ m s}^{-2}$
Mantle thickness	$D$	1	2890 km
Thermal expansivity	$\alpha_0$	-	$3 \times 10^{-5} \text{ K}^{-1}$
Thermal diffusivity	$\kappa$	-	$10^{-6} \text{ m}^2 \text{ s}^{-1}$
Thermal conductivity	$k$	-	$4 \text{ W m}^{-1} \text{ K}^{-1}$
Gas constant	$R$	-	$8.314 \text{ J mol}^{-1} \text{ K}^{-1}$
Reference density	$\rho_0$	1	$3300 \text{ kg m}^{-3}$
Internal heating rate	$H$	20	$5.44 \times 10^{-12} \text{ W kg}^{-1}$
Reference viscosity	$\eta_0$	1	$6 \times 10^{22} \text{ Pa s}$
Activation energy	$E_a$	8	$170 \text{ kJ mol}^{-1}$
Activation volume	$V_a$	3	$6.34 \cdot 10^{-7} \text{ m}^3 \text{ mol}^{-1}$
Surface temperature	$T_s$	0.12	300 K
Superadiabatic temperature drop	$\Delta T$	1	2500 K
Rayleigh number	Ra	$10^6$	-
Surface yield stress in oceans	$\sigma_0$	$10^3$ to $8 \times 10^3$	7 MPa to 56 MPa
Yield stress depth derivative in oceans	$\sigma'_Y$	$3.3 \times 10^5$	$810 \text{ Pa m}^{-1}$

**Table 1.** Dimensional and non-dimensional parameters of the convection model.

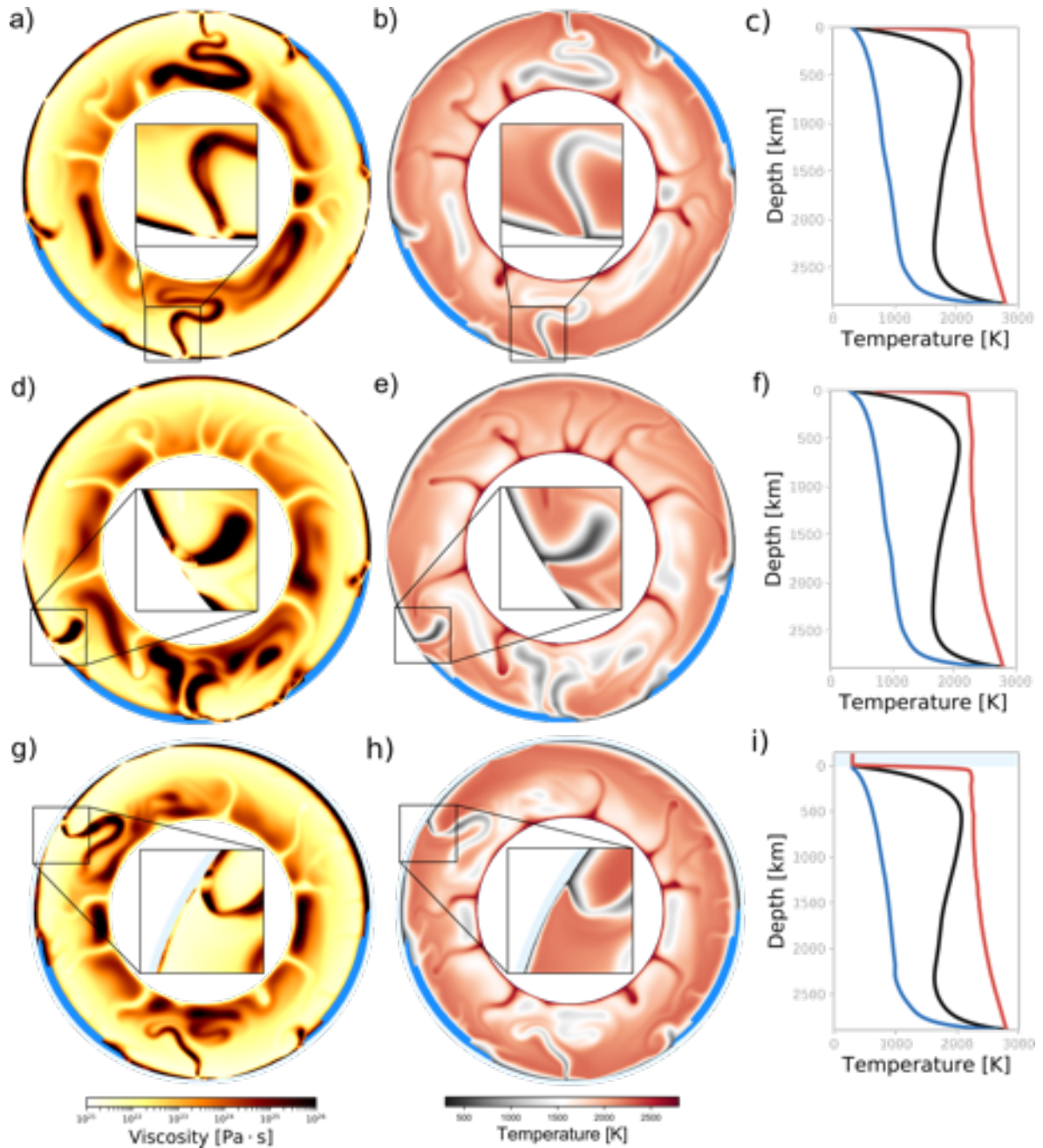


**Figure 1.** A snapshot of the viscosity (left column) and temperature (middle column) fields at one particular time. (Right column) Azimuthally and temporally averaged temperature profiles of minimum (blue), mean (black) and maximum (red) temperature. Model without a)–c) and with d)–f) weak crustal layer. g)–i) Model with free surface. Air layer atop of the mantle is shown in light blue. Continents are emphasized in all panels in blue.

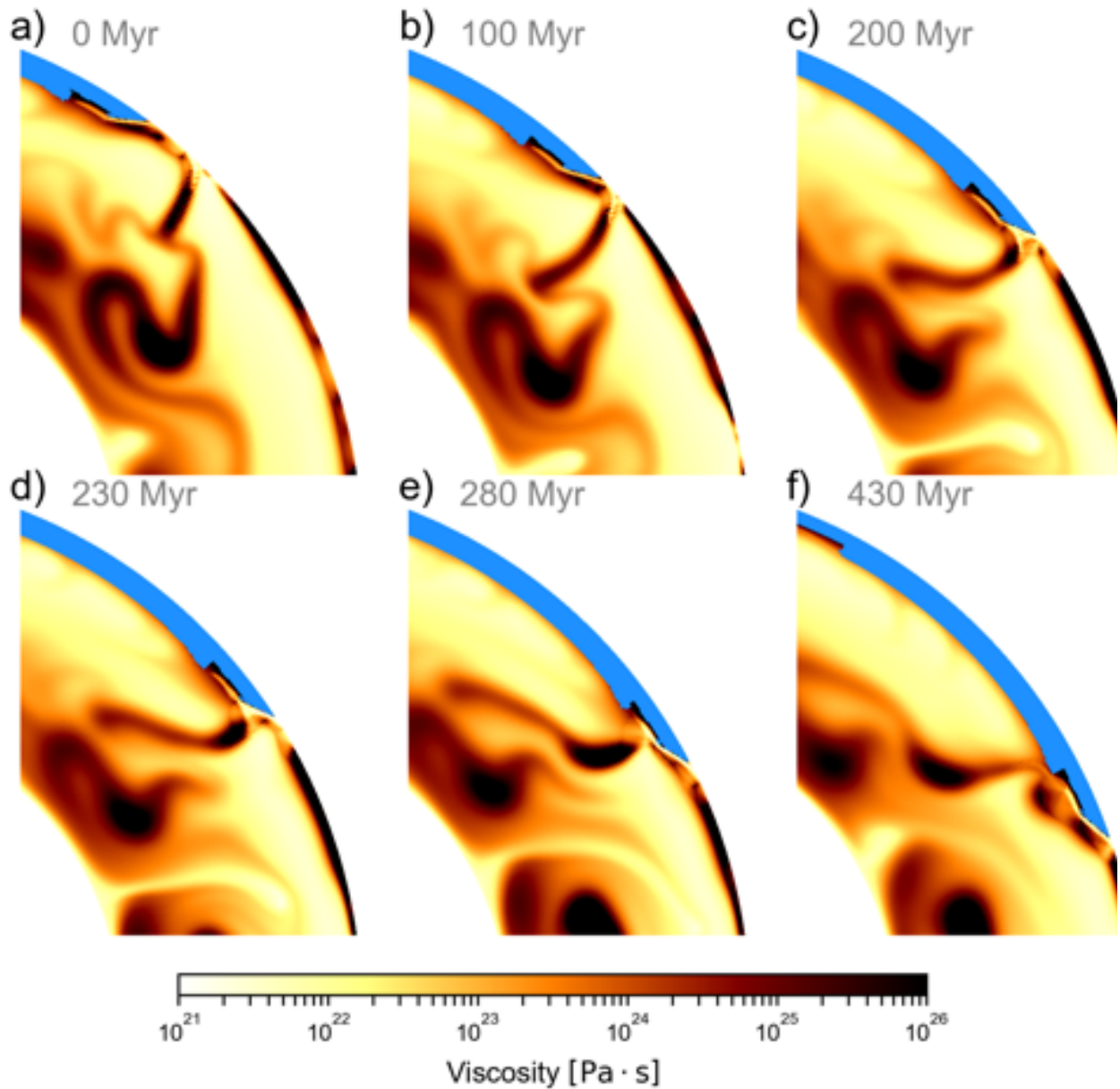


**Figure 2.** a)-c) Subduction zone retreating toward the continent (emphasized in blue) and reaching the continental margin. d)-f) Subduction zone changes its polarity and continues descending into the mantle next to the margin. The model has a weak crustal layer and intermediate yield stress  $\sigma_0 = 35$  MPa.

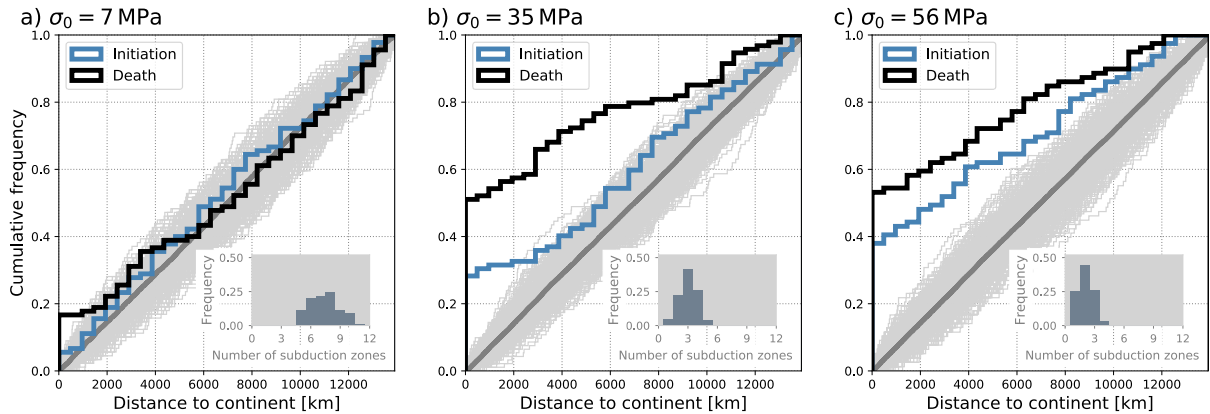


**Figure 3.** Cumulative distribution of subduction initiation (blue) and cessation (black) as a function of distance from the nearest continent for three different yield stresses  $\sigma_0$  (increasing from left to right). Dark grey line represents the distribution of subduction initiation at random position for a large population of cases. Gray area designates random distributions generated for  $N$  subduction initiations with  $N$  being the number of initiations detected for a particular model. Number of subduction zones detected is (from left to right) 89, 93 and 78. Histograms in the bottom right corners show the distribution of the number of subduction zones in the respective models. The models have a free slip top boundary but no weak crustal layer.

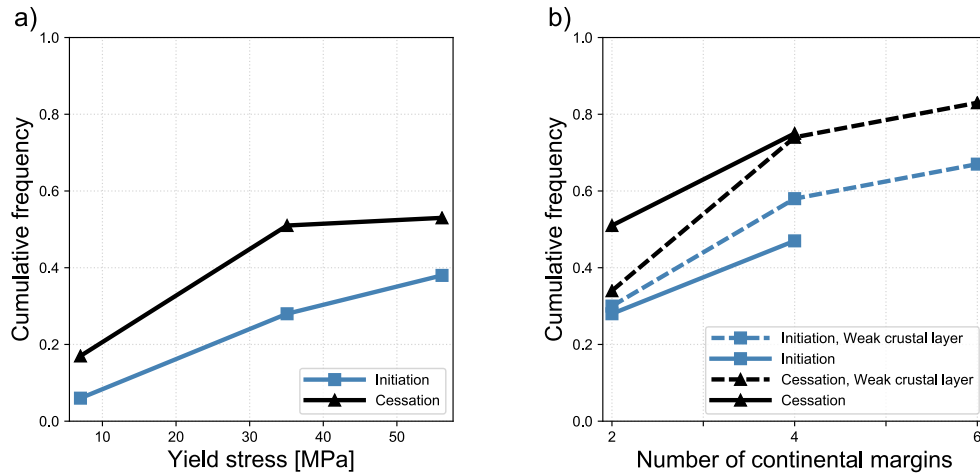


**Figure 4.** a) Proportion of all subduction zones that initiate (blue) and cease (black) in the vicinity of the continent as a function of the lithospheric strength. One continental raft is present (i.e., two margins) throughout the simulations. b) Proportion of all subduction zones that initiate (blue) and cease (black) in the vicinity of the continent as a function of the number of the continental margins. Solid line is for models with compositionally uniform oceanic lithosphere while dashed line is for runs with weak crustal layer. The yield stress is fixed at  $\sigma_0 = 35$  MPa.

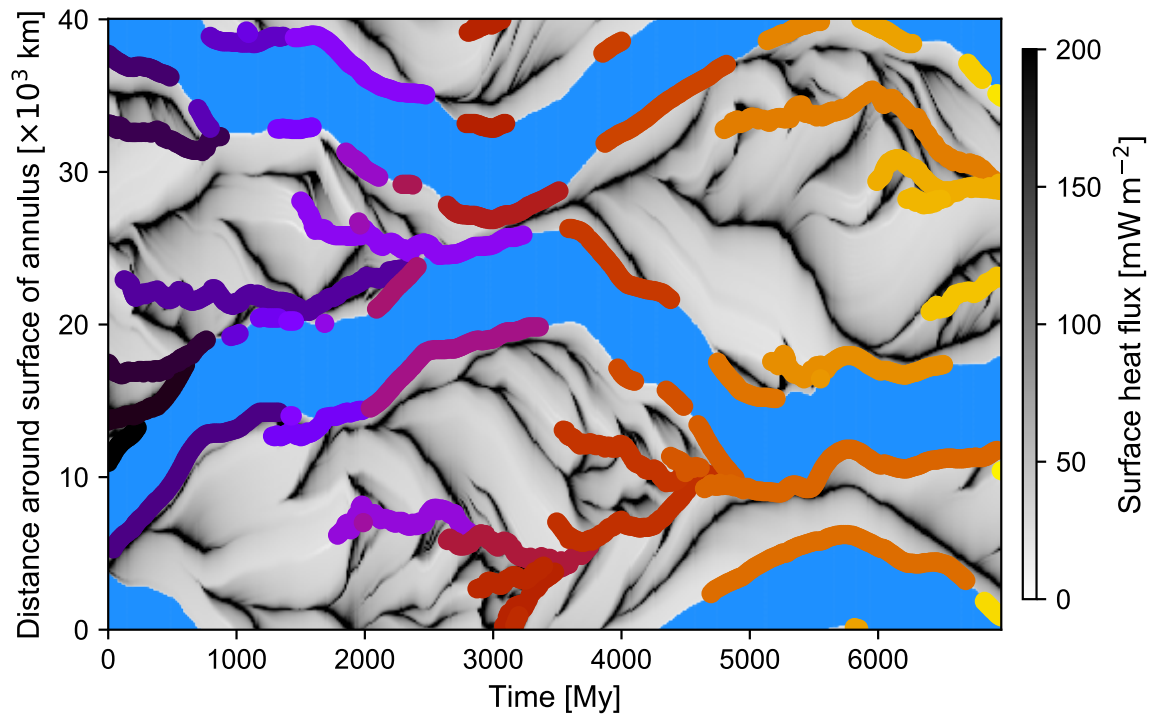


**Figure 5.** Position of the continents (blue) and subduction zones (coloured lines; one colour corresponds to individual subduction zone) through time together with the surface heat flux (gray scale). The model has a weak crustal layer and intermediate yield stress  $\sigma_0 = 35$  MPa.

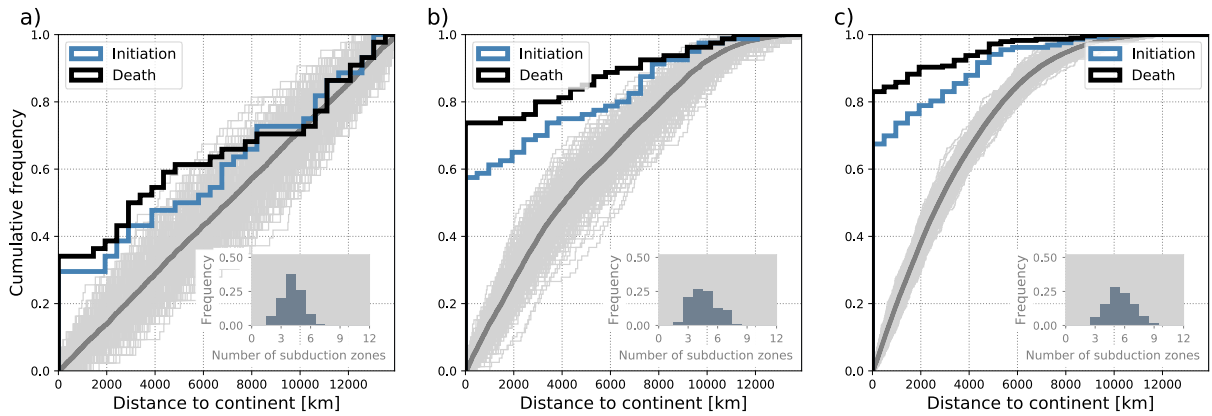


**Figure 6.** The influence of the number of continental margins (increasing from left to right).

a) Two continental margins ( $N = 43$ ), b) four continental margins ( $N = 79$ ), c) six continental margins ( $N = 288$ ).  $N$  is the number of initiations detected for a particular model. Dark grey line represents the distribution of subduction initiation at random position for a large population of cases. Gray area designates random distributions generated for  $N$  subduction initiations. Histograms in the bottom right corners show the distribution of the number of subduction zones in the respective models. The yield stress is  $\sigma_0 = 35$  MPa and the models feature a weak crustal layer.

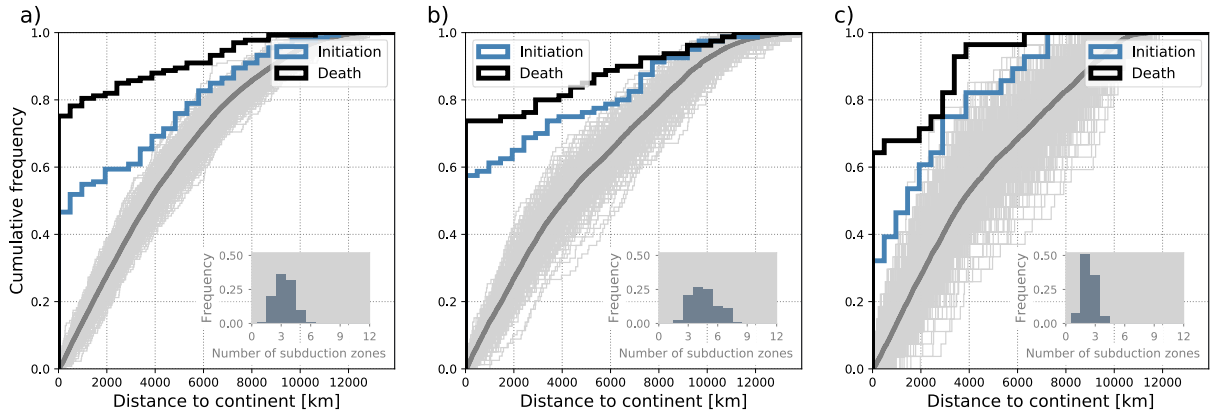


**Figure 7.** Cumulative distribution of subduction initiation (blue) and cessation (black) for model with a) no weak crustal layer ( $N = 132$ ), b) weak crustal layer ( $N = 79$ ), and c) free surface ( $N = 27$ ).  $N$  is the number of subduction initiations detected for a particular model. Dark grey line represents the distribution of subduction initiation at random position for a large population of cases. Gray area designates random distributions generated for  $N$  subduction initiations. Histograms in the bottom right corners show the distribution of the number of subduction zones in the respective models. The yield stress is fixed at  $\sigma_0 = 35$  MPa. There are two continents throughout the simulations.



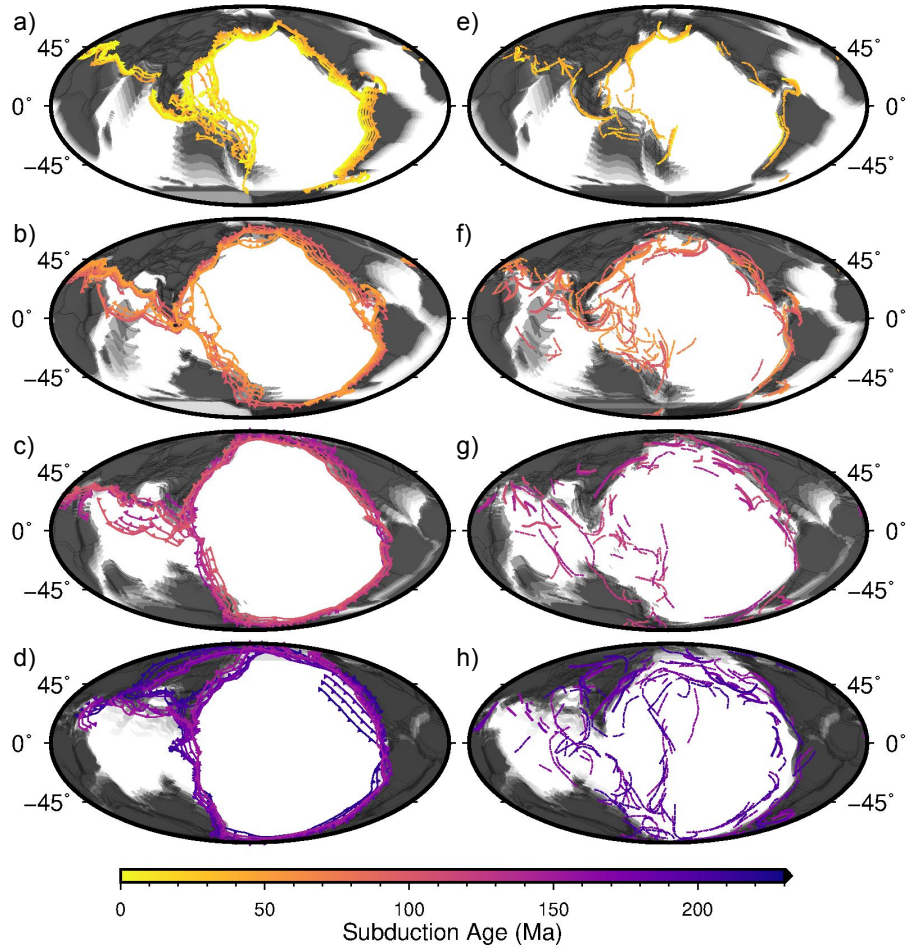


**Figure 8.** Position of the continents and subduction zones since the Triassic according to two alternative reconstructions (see text), subdivided into 4 distinct time windows from Pangea times to recent. The detailed time-evolution of these reconstructions is illustrated in animations S2-S3. a) Subduction zones and continent positions for the M2016 model between 0 and 50 Ma, plotted at 10 Myr increments; locations of subduction zones are shown in colours corresponding to the color legend, while the continents are shown in gray with darker gray standing for younger positions within the 0-50 Myr period. b) same as a for 50-100 Ma; c) same as a for 100-150 Ma; d) same as a for 150-230 Ma; e) V2012 model for times between 0-50 Ma f) same as e for 50-100 Ma; g) same as e for 100-150 Ma h) same as e for 150-235 Ma.

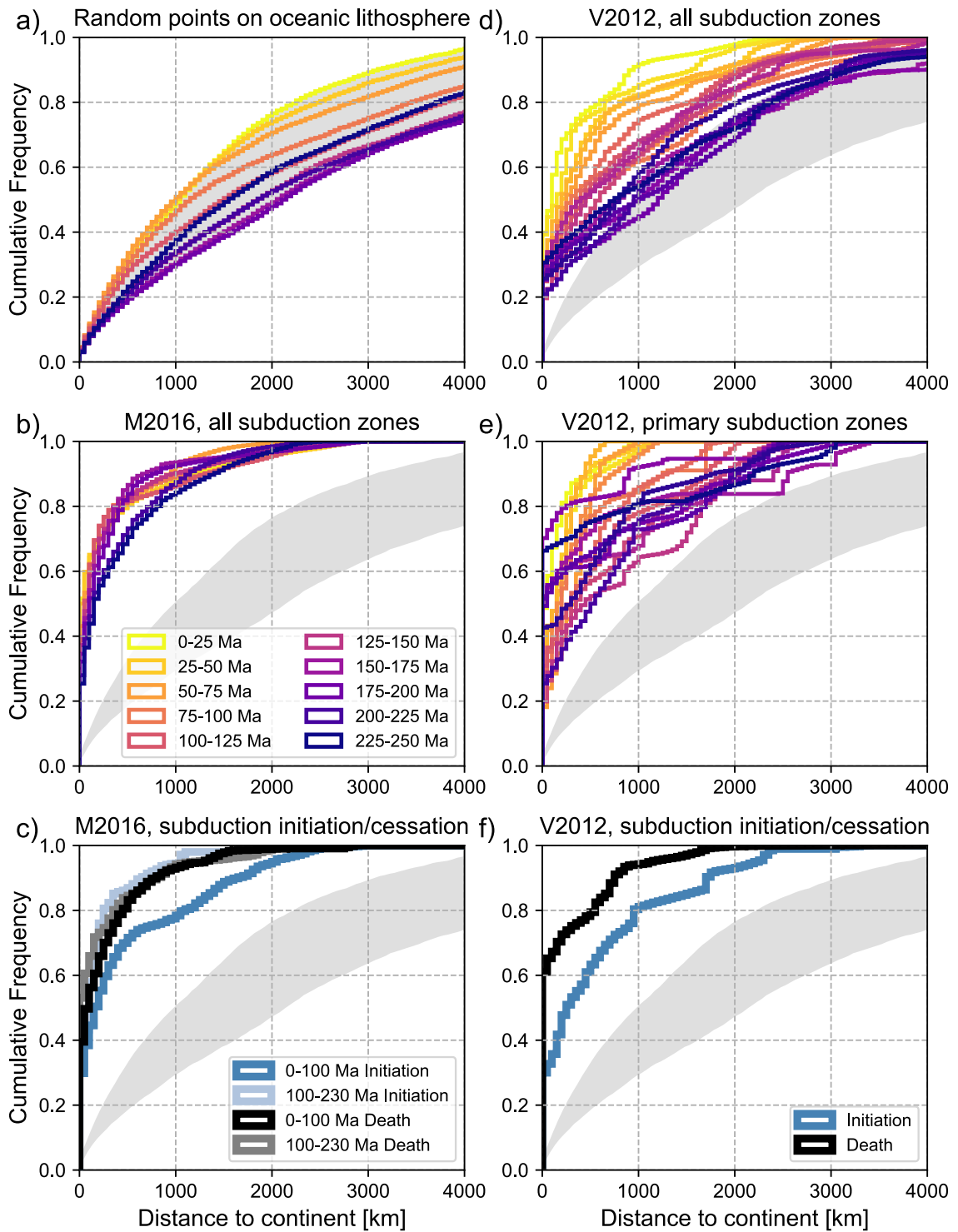


Figure 9. Caption on the next page

**Figure 9.** Cumulative distribution functions for distance between continents and points along subduction zones at different stages of their development for reconstructions from the Triassic to present (see supporting text and animations S2-S3). Each coloured line represents the distribution for a specific time in panels a, b, d and e. In panels c and f, the relatively small number of initiating and ceasing subduction segments are subdivided into broad time ranges encompassing the earlier and later stages of Pangea breakup. See text for further explanation. (a) CDF for random points falling within reconstructed extent of ocean basins; the grey background shows the envelope of these distributions based on random points, and is reproduced on the other panels for visual reference; (b) distance to continent for segments of active subduction zones for the kinematic reconstruction of Müller et al. [2016]; (c) distances to continent for initiating and ceasing subduction segments derived from Müller et al. [2016]; (d) distance to continent for remnants of past subduction mapped from seismic tomography [van der Meer et al., 2010, 2012]; (e) As (d), but only including 'primary' subduction according to the definition of van der Meer et al. [2010]; (f) distance to continents for subduction zones in (e) at the beginning and end of their lifespans (assumed to approximate initiation and cessation) for the slab remnant reconstruction.